ACS APPLIED POLYMER MATERIALS

pubs.acs.org/acsapm

Article

Fast and Straightforward Synthesis in Molecular Imprinting: Core−Shell Polymerization of Magnetic Imprinted Polymers by Microwave Induction

Miriam Guadaño-Sánchez, Fernando Navarro-Villoslada, Guiomar Delgado-Soria, José. F. Marco, Matilde Saura-Muzquiz, Laura Álvaro-Gómez, Patricia de la Presa, Lucas Pérez,* and Javier Lucas Urraca*

Cite This: ACS Appl. Polym. Mater. 2024, 6, 3243−3252

Read Online

ACCESS | Metrics & More | Article Recommendations | Supporting Information

ABSTRACT: In this work, we report a simple and effective approach for preparing molecular imprint polymer (MIP) coatings directly on magnetic multicore (MMC) iron oxide nanoparticles using a microwave reactor to trigger the polymerization reaction. The nanoparticles were manufactured using a microwave reactor, and the MIPs were synthesized with rhodamine 6G (R6G) as the template molecule, methacrylic acid as the functional monomer, and ethylene glycol dimethacrylate as the cross-linker. The produced MMCs and MMC-MIPs were extensively characterized by analysis of powder X-ray diffraction data, Fourier transform infrared spectra, Mossbauer spectroscopy, SQUID magnetometry, and transmission electron microscopy (TEM). The results show the effective formation of the polymeric layer on the surface of the MMCs, without alteration of the structure or physical properties of the core magnetic nanoparticles. The synthesized MIPs presented a high efficiency in the imprinting process of the MMC-MIPs and high selectivity (MIP R6G, $K_a = 7.31 \times 10^{-2}$ M^{-1} y, $\bar{N} = 14.14$ μmol g^{-1}) toward the target molecule R6G.

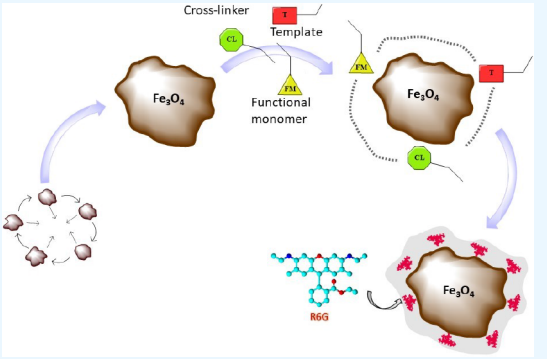

KEYWORDS: *molecularly imprinted polymers, magnetic nanoparticles, microwave-induced polymerization, fluorescence, core−shell nanoparticles*

INTRODUCTION

Molecular imprinting takes place by polymerization of functionalized and cross-linking monomers by the presence of a template molecule, which may be the analyte or a different molecule with similar characteristics to the analyte. After removal of the template, the resulting material contains molecularly imprinted cavities with a size, shape, and distribution of functional groups complementary to the target compound. Molecularly imprinted polymers (MIPs) are artificial recognition units capable of replacing enzymes, antibodies, enzymes, and other bioreceptors in biomimetic sensors, chromatography,[1,2] controlled drug delivery,[3] and catalysis.[4] They potentially offer the specificity and selectivity of biological receptors but with the clear advantages of durability concerning environmental conditions, long-term stability, resistance to organic solvents, and low cost.[5]

Some techniques used today to produce MIP-based nano- and microstructures are grafting and in situ polymerization, microcontact,[6] lithography,[7] photolithography,[8] electro-polymerization,[9] suspension and dispersion polymerization,[10] drop-, dip-, or spin-coating,[11] mechanical microspotting, soft-lithography, e-beam, and electrospinning.[12]

Free radical polymerization, thermal or photochemical initiation, and controlled/living radical polymerization (CRP) techniques are commonly used for polymerization in magnetic cores.[13,14] Free radical polymerization does not allow for control of neither the size of the polymer formed nor the structure to be under control. Therefore, it cannot ensure that the polymerization is solely around the magnetic nanoparticles. On the contrary, CRP polymerization produces much more controlled polymeric network structures and more efficient properties in the magnetic cores. Nevertheless, this polymerization involves several synthesis steps, making it slower than conventional free radical polymerization. Magnetic multicore nanoparticles (MMCs) are magnetic particles of several individual crystalline domains, each of them within the magnetic single domain size region. These domains cause

Received: December 15, 2023
Revised: February 8, 2024
Accepted: February 8, 2024
Published: March 5, 2024

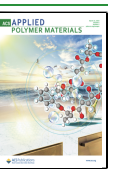

https://doi.org/10.1021/acsapm.3c03068
ACS Appl. Polym. Mater. 2024, 6, 3243−3252

MMCs to exhibit a higher particle magnetic moment than single-core particles, thus improving the magnetic properties of the nanoparticles, such as the higher heating efficiency shown by MMCs.[15,16] The final shell of the polymeric material covers multicore magnetic nanoparticles, which typically have a hydrodynamic diameter of 80−150 nm and contain a magnetic core consisting of a cluster of individual magnetite (Fe_3O_4) or maghemite (Fe_2O_3) domains with a diameter of 5−20 nm each.[17]

Nanocomposite MIPs can be produced by introducing an inorganic material such as supermagnetic iron oxide cores, quantum dot (QD) microcrystals, and metallic nanoparticles (NPs) into the polymer matrix to provide additional properties such as magnetic susceptibility or luminescence, thereby broadening the use of MIPs to different applications.[18] Traditionally, MIPs have been used as sorbent materials for many applications such as solid phase extraction (MISPE), sensors, and catalysts. Nevertheless, these materials generally need to be packaged in a cartridge or reactor, where the recognition of the target molecule will take place. This fact makes it common to find problems of overpressure and blockages within both "off-line" and "on-line" systems. An excellent solution to these problems is the creation of "core−shell" particles where the core is a magnetic material. Thus, when the material bears magnetic properties, it is much more easily manipulated and thereby, these types of problems can be avoided. To do this, it is advisible to use MMC as the core of the composite as they are more easily attracted to a magnet. Thus, MIP nanocomposites with iron oxide nanoparticles are particularly encouraging because magnetic fields allow for a faster, more selective, and efficient extraction of the nanocomposites than traditional centrifugation or filtration methods.[19−22] Unfortunately, it is often easy to observe, during the polymerization process, the formation of agglomerates that substantially reduce the surface area of molecular recognition. For this reason, it is necessary to develop new polymerization methodologies that allow the selective coating of individual particles in this process.

This work presents a method for developing molecularly imprinted polymers on the surface of magnetic multicore nanoparticles (MMC-MIPs) using inductive heating to trigger polymerization. The process involved using microwaves to create hot spots around the iron oxide-based MMCs in the solution containing the prepolymerization mixture and stirring to avoid agglomeration. The conditions such as volume of porogen, time, or power (temperature) were thoroughly controlled in contrast with conventional polymerization with microwaves (MWs). MMCs were selectively heated by MW which caused the formation of a thin layer of MIP on their surface without altering the structure of the coated nanomaterial or the properties of the MIP coating. MIPs were synthesized from rhodamine 6G (R6G) as a template molecule (Figure S1) and methacrylic acid (MAA) as a functional monomer, resulting in well-defined and high-affinity binding sites in the polymeric network via noncovalent interactions between the acid group of MAA and the amino groups of R6G.[23] As a cross-linking monomer, ethylene glycol dimethacrylate (EDMA) was selected, and acetonitrile was employed as porogen. Additionally, nonimprinted magnetic multicore nanoparticles (MMC-NIPs) were prepared in the absence of the template molecule.

EXPERIMENTAL METHOD

Materials. Sodium acetate, ethylene glycol dimethacrylate (EDMA), poly(ethylene glycol) (PEG, Mn 400), methacrylic acid (MAA), and iron(III) chloride hexahydrate ($FeCl_3{\cdot}6H_2O$) were from Sigma-Aldrich. Acetonitrile (AcN; HPLC-grade) was supplied by Honeywell Riedel. Trifluoroacetic acid (TFA, peptide grade) was from Fluorochem. 2,2-azobis(2,4-dimethylvaleronitrile) (ABDV) was from Wako Specialty Chemicals. Ethylene glycol (extra pure) was from Scharlau. Methanol (MeOH, HPLC-grade) was from Fisher Scientific, and rhodamine 6G (R6G) and fluorescein were supplied by Acros (Geel, Belgium).

Synthesis of the Magnetic Multicore (MMC) Nanoparticles. Fe_3O_4-based MMCs were synthesized using a microwave reactor. Briefly, 0.675 g $FeCl_3{\cdot}6\ H_2O$ was mixed with 1.8 g sodium acetate and 20 mL of ethylene glycol in a beaker and stirred vigorously until completely dissolved. Then, 0.45 mL of poly(ethylene glycol) was added, and the solution was stirred at room temperature for 30 min and placed in a microwave reactor where the reaction was carried out at 200 °C for 8 min by continuous stirring at 1200 rpm. The nanoparticles produced were then ultrasonically washed with methanol (2 × 250 mL) and water (2 × 250 mL), isolated with a magnet and dried at 60 °C for 16 h. Distribution size was calculated using ImageJ software, taking 100 particle images.

Synthesis of the MMC-MIP Nanoparticles. The molar ratio of the template molecule (rhodamine 6G), functional monomer, and cross-linker in the MIP was 0.5:2:20. In a 10 mL microwave reaction vial, 10 mg MMCs and 5 mL acetonitrile were added and sonicated for 15 min. Then, the template molecule (R6G, 0.059 mmol), functional monomer (MAA, 0.24 mmol), cross-linker (EDMA, 2.38 mmol), and a glass-coated magnet were added. The reaction mixture was purged with nitrogen for 5 min, and 30 mg of the initiator (ABDV) was added and purged for another minute with nitrogen. The reaction was carried out in a microwave reactor (Anton Paar, model 200) using the following procedure: (I) heating to 30 °C; (II) 30 °C for 1 min at 1200 rpm; (III) heating up to 35 °C; (IV) polymerization at 35 °C for 20 min at 1200 rpm; (V) cooling of the sample. The obtained MMC-MIPs were washed six times with a methanol−water mixture (80:20%v/v) using an ultrasonic bath until no elution of the template was observed by HPLC-FLD. The particles were isolated with a magnet and dried in an oven at 60 °C for 16 h. A nonimprinted polymer (NIP) was synthesized similarly without adding the template molecule.

Chromatographic Analysis. The chromatographic system consisted of an Agilent Technologies (Palo Alto, CA) 1100 series high-performance liquid chromatograph (HPLC) equipped with a quaternary pump, in-line degasser, autosampler, automatic injector, column thermostat, and fluorescence (FLD). Analytes were quantified using an Agilent Technologies (Palo Alto, CA) ZORBAX SB-C18 column (150 mm × 4.6 mm, 3.5 μm size). R6G was analyzed isocratically with a mobile phase of 30% water and 70% methanol, both containing 0.1% v/v TFA, whereas fluorescein was analyzed using a gradient from 60% water and 40% methanol, both containing 0.1% v/v TFA, to 100% methanol (0.1% v/v TFA). The analyses were performed at a flow rate of 1 mL min^{-1}, at 32 °C for R6G and 30 °C for fluorescein, respectively. The injection volume was 10 μL, and both analytes were eluted within 15 min. The fluorescence detector was set at $\lambda_{excitation}$ = 538 nm and $\lambda_{emission}$ = 560 nm for R6G and at $\lambda_{excitation}$ = 445 nm and $\lambda_{emission}$ = 510 nm for fluorescein.

Physical Characterization. The structural characteristics and determination of iron oxide phases of the MMCs and MMC-MIPs' samples were carried out by Rietveld analysis of high-resolution powder X-ray diffraction (PXRD) data using the FullProf Suite software package.[24] The samples were packed in glass capillaries of 0.3 mm in diameter, and PXRD data were collected at room temperature using a Malvern PANalytical Empyrean Alpha1 diffractometer equipped with a Mo ($K_{\alpha1+\alpha2}$) source. Using a Mo source instead of a conventional Cu X-ray source avoids unwanted high background in the data due to fluorescence from Fe at the more commonly used Cu X-ray energy. Data were collected in the 2θ range of 2 to 60° (q range

https://doi.org/10.1021/acsapm.3c03068
ACS Appl. Polym. Mater. 2024, 6, 3243−3252

of 0.35−8.84 $Å^{-1}$), with a step size of 0.0084°. Spinning of the capillary was carried out during data collection to avoid preferred orientation effects. The peak profile was modeled using the Thompson-Cox-Hastings formulation of the pseudo-Voigt function.[25] The Thompson−Cox−Hastings instrumental resolution function was determined by performing a LeBail fit of a NIST LaB_6 660b standard, measured under the same conditions as the studied samples. This function was implemented in the refinements of the studied materials to deconvolute the instrumental and sample contributions to the peak width, thereby obtaining accurate crystallite sizes.

Mossbauer spectrometry was used to further study the iron oxide phases of the synthesized samples. ^{57}Fe Mössbauer data were recorded in the transmission mode using a conventional constant spectrometer and a ^{57}Co(Rh) source. Low-temperature data were recorded using a He closed-cycle cryorefrigerator. The velocity scale was calibrated using a 6-μm thick α-Fe foil. The chemical isomer shifts were referred to the centroid of the spectrum of α-Fe at room temperature.

The morphology of the MMCs and MMC-MIPs was examined with a JEOL JEM 1400 transmission electron microscope (TEM) operating at 300 kV. Before measurements, the samples were dispersed in methanol, and a drop of the resulting colloid was deposited on copper grids coated with carbon holey films. To corroborate the formation of the polymer layer on the surface of the magnetic NPs, Fourier transform infrared (FTIR) spectra of the MMCs and MMC-MIP were performed.

Equilibrium Binding Experiment. For the absorption kinetics, 8 mg of MIP/NIP MMC were placed into 2 mL HPLC vials with 1 mL of a 225 μM R6G solution in acetonitrile. The suspension was kept under continuous stirring. After the incubation step, the concentration of the bound analyte was calculated by subtracting the free analyte from the original concentration. This free analyte remaining in the supernatant was determined by HPLC-FLD. Thirteen experimental points were recorded for each polymer between 2 and 140 min. In the adsorption isotherm, 8 mg of MIP/NIP-MMC were weighed and mixed with 1 mL of acetonitrile containing increasing concentrations of fluorescein in 10−500 μM and stirred at room temperature in the dark for 24 h.

All cross-reactivity assays with fluorescein, methylene blue, and curcumine were performed in triplicate at a concentration of 200 μM and incubated with the MMC-MIP and MMC-NIP nanocomposites for 24 h, after which the supernatants were extracted and measured by HPLC for quantification purpose. The corresponding amounts of analyte retained by the polymers were calculated by difference of the values of 200 μM standard solutions less the concentration present in the supernatants after incubation.

Magnetic Characterization. A superconducting quantum interference device from Quantum Design (San Diego, CA) was used to assess the magnetic properties of the nanoparticles before and after polymerization. Hysteresis loops were measured at room (300 K) and low (10 K) temperature. The thermal dependence of magnetization was also assessed under field-cooled (FC) and zero-field-cooled (ZFC) conditions with a magnetic field of 100 Oe for both cooling and measuring.

RESULT AND DISCUSSION

Optimization of the MMC-MIP Nanoparticle Synthesis. A statistical response surface modeling approach based on a face-centered central (FCC) composite experimental design was applied to optimize the experimental parameters that may affect the thickness of the polymeric layer on the surface of the MMC. The selected parameters were reaction temperature, reaction time, and solvent volume, where the experimental domain used to study the effect of the parameters was 35−55 °C, 10−20 min, and 1.5−5 mL, respectively. The molar ratio of the template molecule (rhodamine 6G), functional monomer, and cross-linker in the MIP was set to 0.5:2:20.

A total of 19 polymerization runs were performed, i.e., 8 factorial points, 6 axial points and 5 replicas of the central point, with the MIP nanoshell thickness, estimated from the TEM images, being the target response (Table S1). The average MIP thickness for each experimental run was estimated by measuring the MIP thickness in different regions of the nanoparticles in the TEM image and applying a robust method (algorithm A) advocated by the International Organization for Standardization.[26] MIP thickness in the experimental domain selected ranged from 5.5 to 25.4 μm.

The TEM micrographs showed significant morphological differences in the MIP thickness depending on the working conditions. Response surface models relating MIP thickness to reaction temperature, reaction time, and solvent volume were estimated using the ordinary least-squares methodology. All possible interactions between the three parameters were initially considered, selecting the significant coefficients of each empirical model by the stepwise regression technique and the p-value criteria, setting the thresholds for adding and removing coefficients 0.1. The models' significance and lack of fit were checked by an Analysis of Variance (ANOVA). All the models were significant at $p < 0.01$ with a significant lack of fit ($p > 0.05$).

Three diagnostic plots were also used to assess the adequacy of the empirical models: (i) a normal probability plot of the Studentized residual, (ii) studentized residuals versus predicted values, and (iii) predicted versus actual response values. The normal probability plot of the studentized residuals shows a linear correlation consistent with an assumption of normally distributed errors (Figure S2). In contrast, the studentized residuals versus the predicted values showed no unusual observations or trends, being all the values randomly distributed around zero. A scatter plot of predicted and actual MIP thickness and RSD values showed a good agreement between both (Figure S3).

Figure 1 shows the response contour plots for the fitted model obtained for the MIP thickness on the surface of the MMC nanoparticles. The empirical model revealed a positive interaction of the solvent volume with the reaction temperature and the reaction time on the MIP thickness. Thus, MIP thickness increased with increasing reaction temperature, reaction time, and solvent volume. Nevertheless, in these working conditions, a significant particle aggregation was observed. Since the objective was to achieve a suitable MIP thickness with as little particle aggregation as possible, the working conditions were set to 35 °C, 20 min, and 5 mL for the reaction temperature, reaction time, and solvent volume, respectively.

Structure and Morphology of the Nanoparticles. The atomic, nano and microstructure of the MMC-MIP and MMC-NIP nanoparticles were characterized by powder X-ray diffraction (XRD), TEM, and FTIR, and their efficiency in the selective extraction of R6G was evaluated based on equilibrium rebinding measurements.

The two archetypical spinel iron oxides, i.e., magnetite (Fe_3O_4) and maghemite (γ-Fe_2O_3), adopt very similar structures. They both crystallize in the spinel-type structure, in space group $Fd\bar{3}m$, which consists of a fcc oxygen lattice with tetrahedral (8a) and octahedral (16d) iron sites. What differentiates the structures is that, while γ-Fe_2O_3 contains only Fe^{3+} ions, in Fe_3O_4, both Fe^{3+} and Fe^{2+} are present. To keep charge neutrality in γ-Fe_2O_3, 16.67% vacancies are introduced in octahedrally coordinated iron site. In addition to these two

https://doi.org/10.1021/acsapm.3c03068
ACS Appl. Polym. Mater. 2024, 6, 3243−3252

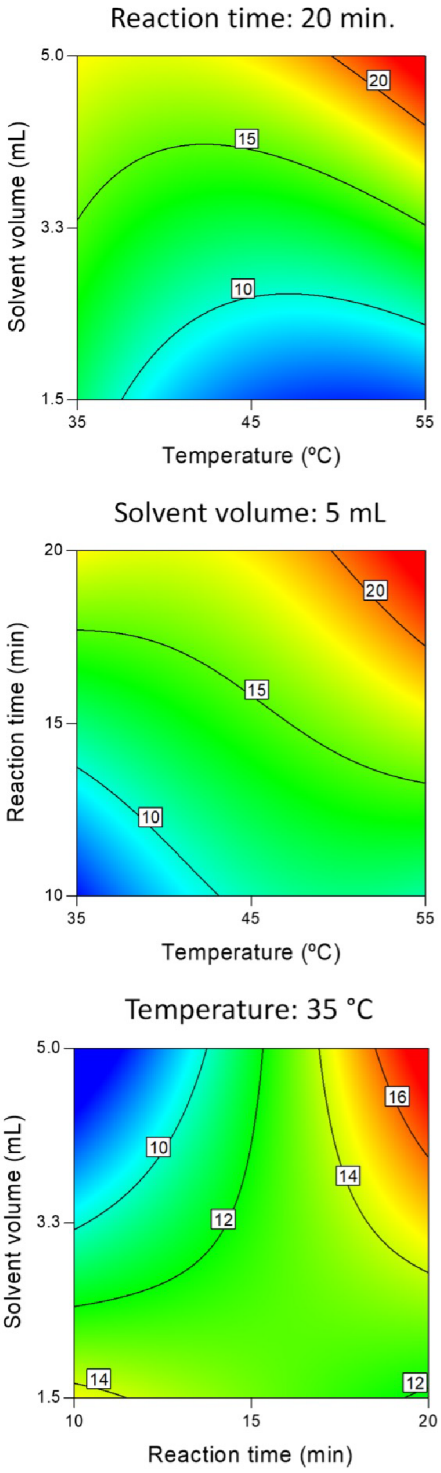

Figure 1. Response contour plots for the empirical model estimated by fitting the thickness of the MIP layer data as a function of the reaction temperature, reaction time, and solvent volume.

end-member compositions, the spinel iron oxide can also exist in nonstoichiometric compositions, i.e., Fe_xO_4 where $x = 3 - \delta$. Here, the amount of iron vacancies (δ) adopts a value between zero, as for Fe_3O_4, and 0.333, as for γ-Fe_2O_3. As a result, the Fe/O ratio varies from 0.75 in Fe_3O_4 to 0.6667 in γ-Fe_2O_3 and exhibits a value in between in nonstoichiometric Fe_xO_4 species. In some cases, ordering of vacancies in γ-Fe_2O_3 takes place, leading to a modification of the structure. This phenomenon has been extensively studied in bulk materials and, as a result, over the last few decades, the structure of γ-Fe_2O_3 has been reported in several space groups.[27−29] Observation of vacancy order in γ-Fe_2O_3 nanoparticles is challenging, due to the broad nature of the diffraction peaks. However, a recent in-depth study of the structure of iron oxide nanoparticles was carried previously[30] combining synchrotron PXRD and neutron powder diffraction data analysis, pair distribution function (PDF) analysis, Mössbauer analysis, and transmission electron microscopy. Their study showed that iron oxide nanoparticles with crystallite sizes between 10 and 25 nm were best described by γ-Fe_2O_3 with vacancy ordering, in tetragonal space group $P4_32_12$.

The structures of magnetite, maghemite, and vacancy ordered γ-Fe_2O_3 in $P4_32_12$ are illustrated in Figure 2, with the octahedral sites where vacancies are located emphasized in blue. It should be noted that nonstoichiometric Fe_xO_4 structures have a structure equal to that of maghemite (Figure

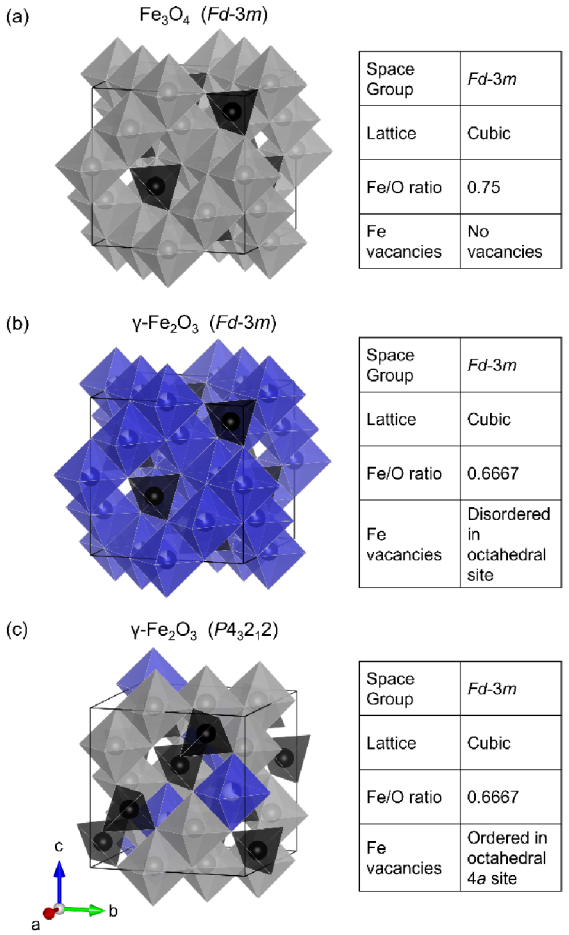

Figure 2. Illustration of the structure of (a) magnetite Fe_3O_4, (b) maghemite γ-Fe_2O_3, and (c) vacancy ordered γ-Fe_2O_3 in space group $P4_32_12$. The gray and black polyhedra represent octahedrally and tetrahedrally coordinated iron, respectively. The oxygen atoms (not shown) are located at the vortices of the polyhedra. The blue polyhedra highlight partially unoccupied octahedral sites, illustrating the lack (a) or presence (b,c) of vacancies in the different structures and whether they are disordered (b) or ordered (c). The degree of occupation on the blue octahedral sites is represented by the blue wedge of the sphere inside the polyhedra.

https://doi.org/10.1021/acsapm.3c03068
ACS Appl. Polym. Mater. 2024, 6, 3243−3252

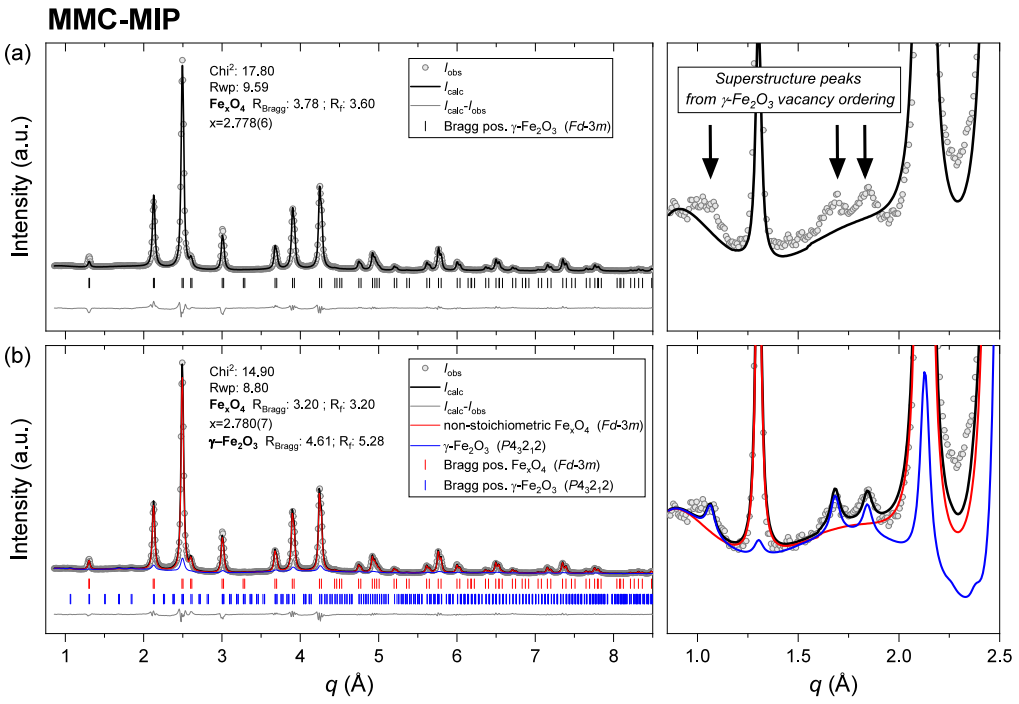

Figure 3. Rietveld refinement of PXRD data collected on the MMC-MIP sample modeled using (a) the nonstoichiometric Fe_xO_4 and (b) a combination of Fe_xO_4 and vacancy ordered γ-Fe_2O_3 in space group $P4_32_12$. The right-hand side plots show the superstructure peaks at the low q-region of the pattern.

2b), but with different degree of Fe occupation on the octahedral (blue) sites.

Although the differences in PXRD data between the different iron oxide structures are subtle and are often misinterpreted or disregarded in literature, distinguishing between the different structures is possible if high-quality data are collected. The PXRD patterns of magnetite and maghemite differ in the relative peak intensities due to the different ratio between Fe and O. Additionally, when vacancy ordering takes place, as is the case for γ-Fe_2O_3 in space group $P4_32_12$, it leads to the emergence of weak superstructure peaks in the diffraction pattern.

To unequivocally determine which iron oxide phase our multicore nanoparticles consist of, high-resolution PXRD data were collected using a Mo ($K_{\alpha 1+\alpha 2}$) X-ray source. Conventional Cu sources lead to Fe fluorescence and hence a high background in the data. For samples with high Fe content, that gives rise to a poor signal-to-noise ratio, hides low-intensity peaks, and hinders the structural analysis of the material. The use of a Mo source eliminates fluorescence from Fe and allows for the observation of subtle features such as small changes in peak intensity or weak superstructure peaks.

The collected PXRD data of both, MMC and MMC-MIP samples, were refined using three different models: the magnetite Fe_3O_4, the maghemite γ-Fe_2O_3, and a non-stoichiometric Fe_xO_4 structure (Figures S4 and S5). In both cases, modeling of the data using the magnetite or maghemite model did not accurately describe the relative intensity of the diffraction peaks. Refinement of a nonstoichiometric Fe_xO_4 structure yielded the best fit to the data, indicating that this is in fact the structure of the multicore magnetic nanoparticles (see Figures S4 and S5 for refinement plots and reliability factors of the different refinement models). The refined Fe content of the samples (x in Fe_xO_4) was 2.785(6) and 2.778(6) for MMC and MMC-MIP, respectively.

Careful inspection of the data revealed the existence of additional superstructure peaks, which are characteristic of vacancy order in γ-Fe_2O_3. Implementation of a second phase in the structural model, corresponding to that reported before[30] (tetragonal γ-Fe_2O_3 in space group $P4_32_12$) was carried out to fit the observed superstructure peaks. The comparison of the MMC-MIP data analysis using exclusively the Fe_xO_4 model vs the combination of Fe_xO_4 and vacancy ordered γ-Fe_2O_3 is shown in Figure 3. The analysis shows an excellent description of the data, including the superstructure peaks. An equivalent analysis of the MMC sample is shown in Figure S6, confirming that no structural change took place during the polymerization of the magnetic nanoparticles.

The refined value of iron (x in Fe_xO_4) in the final model is 2.793(6) and 2.780(7) in MMC and MMC-MIP, respectively, which are compatible and prove that no change whatsoever takes place in the nanoparticles after polymerization. This value also indicates that the sample is closer to maghemite (where x = 2.6667) than to magnetite (x = 3). The refined weight percentage of each phase is also the same before and after polymerization, having 89.9(8) wt % of Fe_xO_4 and 10.19(6) wt % of vacancy ordered γ-Fe_2O_3. The refined crystallite sizes are 16.0(2) nm for Fe_xO_4 and 8.6(9) nm for γ-Fe_2O_3, indicating that the crystalline domains with vacancy orders are smaller than those with disordered vacancies. This finding is also consistent with the results developed previously.[30]

The room temperature Mössbauer recorded from the MMCs and the MMC-MIP nanoparticles are shown in Figure 4. The spectra are composed in both cases of a broad asymmetric magnetic pattern characteristic of a hyperfine magnetic field distribution associated with a material experiencing superparamagnetic relaxation. The results are consistent with a distribution of particle sizes having different blocking temperatures. The hyperfine magnetic field distribu-

https://doi.org/10.1021/acsapm.3c03068
ACS Appl. Polym. Mater. 2024, 6, 3243−3252

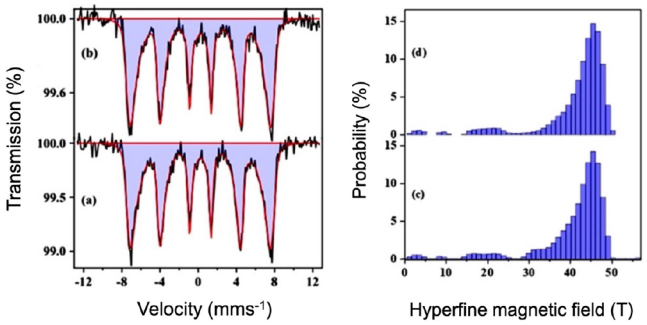

Figure 4. Mössbauer spectra of (a) MMCs and (b) MMC-MIP, and estimated hyperfine magnetic field distribution of (c) MMC and (d) MMC-MIP.

tions obtained from the Mössbauer data fit are shown in Figure 4c and 4d. The hyperfine parameters characterizing both distributions are collected in Table 1.

Table 1. Hyperfine Magnetic Field Parameters of the MMC and MMC-MIP Nanoparticles[a]

	δ (mm s^{-1})	2ε (mm s^{-1})	H_{max} (T)	H_{av} (T)	W (T)
MMC	0.34	0.02	45.6	41.2	8.5
MMC-MIP	0.34	−0.01	46.3	41.2	9.0

[a] δ: isomer shift; 2ε: quadrupole shift; H_{max}: maximum hyperfine magnetic field; H_{av}: average hyperfine magnetic field; W: width of the hyperfine magnetic field distribution.

The spectra and the corresponding distributions are very similar, indicating that the MIP coating of the MMC does not affect their composition or structural characteristics. Spectra like these have been reported for magnetite particles with average diameters ranging between 10 and 17 nm.[31,32]

It is well-known that the Mössbauer spectrum at room temperature of bulk magnetite consists of two well-separated magnetic sextets corresponding, on the one hand, to the Fe^{3+} ions, sitting on the tetrahedral sites of the spinel-related structure and, on the other hand, the Fe^{3+}/Fe^{2+} ions occupying the octahedral sites, their parameters being characteristic of a mixed valent $Fe^{2.5+}$ species due to the occurrence of electron hopping between the Fe^{3+} and Fe^{2+} octahedral cations.[33] For nonstoichiometric iron oxide (Fe_xO_4) particles, like the ones in this study, the Mössbauer spectrum contains three sextets: one for $Fe^{2.5+}$ and two for Fe^{3+} with slightly different isomer shifts and hyperfine field. This means that the Mössbauer spectrum of nonstoichiometric Fe_xO_4 and that of Fe_3O_4 are very similar, only differing in the area ratio of the subspectra. In the case of magnetite nanoparticles, the two sextets at RT are not often observed but rather a broad magnetic pattern as those shown in Figure 4. In the case of our Fe_xO_4 particles, they exhibit a low temperature spectrum with multiple sextets, see Figure 5b, as it is expected for magnetite.[32]

Figure 5 shows the Mössbauer spectra recorded from MMC nanoparticles at room temperature and 8.5 K. The 8.5 K spectrum is much narrower than the room temperature one, and its shape is asymmetric, with the absorption peak at around +4.5 and +8 mm s^{-1} broader than those appearing at around −4.5 and −8 mm s^{-1}, respectively, something that is characteristic of the low-temperature Mössbauer spectrum of magnetite. The spectrum fits well with the five sextets model, and the corresponding hyperfine parameters (see Table 2) are

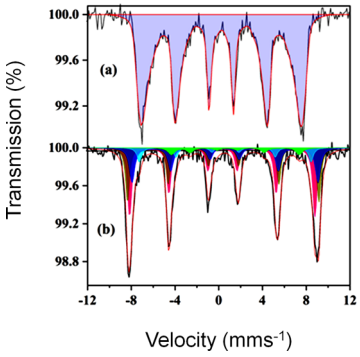

Figure 5. Mössbauer spectra of the MMC nanoparticles recorded at (a) room temperature and (b) 8.5 K.

Table 2. Hyperfine Magnetic Field Parameters and Area of the Components of the Five Sextets Model

component	δ (mm s^{-1})	2ε (mm s^{-1})	H (T)	area (%)
sextet 1	0.33	−0.04	52.5	36
sextet 2	0.42	−0.06	54.1	26
sextet 3	0.56	0.11	52.9	24
sextet 4	0.70	−0.39	48.2	9
sextet 5	1.20	0.70	36.2	5

consistent and within the range of those reported for magnetite nanoparticles of comparable sizes. The chemical composition of the Fe_3O_4-based MMC nanoparticles was determined by FTIR spectroscopy. Figure S5 shows the FTIR spectra of the MMC nanoparticles before and after MIP coating. In the case of the FTIR spectrum of the MMC nanoparticles (Figure S7, red line), the 556 cm^{-1} band was assigned to the Fe−O bond stress vibrations. In contrast, the FTIR spectrum of the MMC-MIP nanoparticles showed a higher significant number of bands (Figure S5, black line). In this case, the 3390 cm^{-1} band was assigned to the tensile vibration of the O−H bonds in the COOH group of the functional monomer, the 2980 cm^{-1} band to the O−H dimer strain, the 1440 cm^{-1} band to the O−H bond twist of the carboxylic acids, the 1020 cm^{-1} band to the symmetric strain of the C−O−C bonds inherent in the polymer chain, and the 1640 cm^{-1} band to the C═C strain by unreacted functional monomers. Thus, the presence of these bands verifies the presence of a polymeric layer on the MMC nanoparticle's surface.

Figure 6 shows the TEM images of the MMC nanoparticles before and after the MIP coating process. Before the polymerization process (Figure 6a, distribution size shown in Figure S8), the micrograph confirms the correct synthesis of

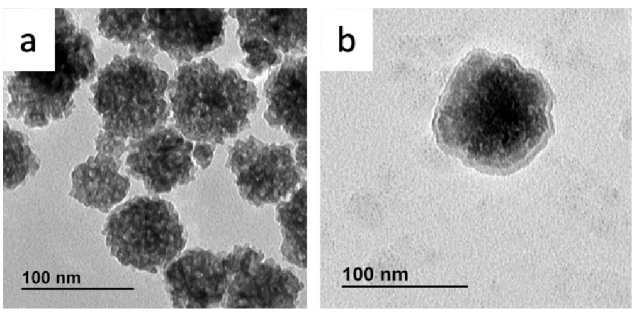

Figure 6. Transmission electron micrographs of the (a) MMC and (b) MMC-MIP nanoparticles.

https://doi.org/10.1021/acsapm.3c03068
ACS Appl. Polym. Mater. 2024, 6, 3243−3252

Table 3. Estimated Pseudo-First- and Pseudo-Second-Order Kinetic Model Parameters

	pseudo-first-order kinetic model				pseudo-second-order kinetic model			
	$[A]_0$ (mg g^{-1})	k_1 x 10^3 (min^{-1})	$t_{1/2}$ (min)	r^2	$[A]_0$ (mg g^{-1})	k_2 (mg $^{-1}$g min^{-1})	$t_{1/2}$ (min)	r^2
MMC-MIP	7.7 ± 0.2	71 ± 5	9.8 ± 0.7	0.97	8.0 ± 0.3	11 ± 2	0.011 ± 0.7	0.96
MMC-NIP	7.4 ± 0.3	200 ± 40	3.5 ± 0.7	0.65	7 ± 1	3 ± 1	0.05 ± 0.01	0.70

the magnetic magnetite nanoparticles of about 70 nm in diameter, formed of smaller crystalline nuclei, which is consisting with the PXRD analysis showing crystalline domains of approximately 16 nm. On the other hand, The TEM image of the MMC-MIP nanoparticles (Figure 6b) clearly shows the formation of a nanosized polymeric layer around the MMC nanoparticles (5−20 nm).

R6G Adsorption Kinetic on MMC-Polymer Coated Nanoparticles. The kinetic curves of R6G adsorption onto MMC-MIP and MMC-NIP nanoparticles were investigated using pseudo-first-order and pseudo-second-order kinetic models to investigate the experimental data (Figure S9). The coefficient of determination (r^2) was the statistical criterion to evaluate the appropriateness of the fitting models. MIP and NIP adsorbed roughly 80% of the initial amount of R6G in 30 and 10 min, respectively.

The pseudo-first-order kinetic model of the adsorption has a rate-limiting diffusion step and follows the equation:

$$[A] = [A]_0 \cdot e^{-k_1 \cdot t} \quad (1)$$

where $[A]$ (mg g^{-1}) is the concentration of R6G adsorbed at time t, $[A]_0$ is the original concentration of R6G, and k_1 (min^{-1}) is the pseudo-first-order kinetic constant.

On the other hand, the pseudo-second-order kinetic model follows the equation:

$$[A] = \frac{[A]_0}{\left(\frac{1}{[A]_0 \cdot k_2 \cdot t}\right) + 1} \quad (2)$$

where k_2 (mg^{-1} g min^{-1}) is the pseudo-second-order adsorption kinetic constant. The adsorption half-life time for both models is calculated from eqs 3 and 4, respectively:

$$t_{1/2} = \frac{-\ln 0.5}{k_1} \quad (3)$$

$$t_{1/2} = \frac{1}{k_2 [A]_0} \quad (4)$$

Table 3 summarizes the kinetic parameters of both fitting models for the adsorption of R6G on the MMC-MIP and MMC-NIP. The coefficient of determination (r^2) for the MMC-MIP nanoparticles showed similar values for the pseudo-first-order and pseudo-second-order models. Therefore, this indicates that various processes, such as chemical adsorption or internal diffusion within the porous material, may govern the adsorption process on the MIP. Although MIP showed higher adsorption capacity than NIP, its adsorption kinetics was slightly slower, which might corroborate the previous observation, as different adsorption mechanisms could limit the adsorption rate. Adsorption on NIP was faster as the amount of R6G adsorbed was roughly half that on MIP, pointing out the selectivity of the binding sites developed on the MIP. The longer adsorption time taken in the MIP suggests a wide distribution of both high- and low-affinity binding sites in the polymer because of the presence of the R6G during the polymerization process.

Binding Characteristics of the MMC-MIP and MMC-NIP Nanoparticles. The binding properties of the MCC-MIP and MMC-NIP nanoparticles were evaluated from equilibrium binding experiments. The binding features of R6G to the MMC-MIP and MMC-NIP nanoparticles were modeled using the Freundlich isotherm model (Figure 7)[34]

$$B = a \cdot F^m \quad (5)$$

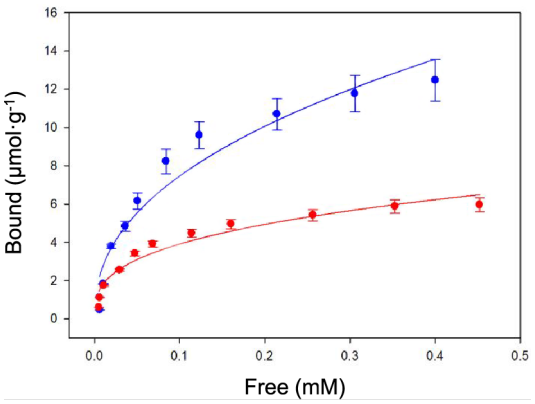

Figure 7. Equilibrium binding experiment for the adsorption of R6G in MMC-MIP (blue line) and MMC-NIP (red line) nanoparticles. Data fitted to a Freundlich adsorption isotherm model. Total number of points: 11 (n = 2).

where B and F indicate the amount of R6G adsorbed on the MMC nanoparticles and free, a is the binding capacity and m is the so-called heterogeneity index. This last parameter takes values from 0 to 1, where values closer to 1 indicate a higher homogeneity in the distribution binding sites.

The affinity constant (K_a) and the total number of binding sites ($\bar{N}$) of the high and low energy binding sites for R6G in the MMC-MIP and MMC-NIP nanoparticles are summarized in Table 4.

The comparison of the binding properties of the polymers shows that the binding capacity and the affinity constant of MMC-MIP nanoparticles are higher than the corresponding MMC-NIP for R6G, i.e., template molecule (i.e., MMC-MIP: 470 μmol g^{-1}; MMC-NIP: 10 μmol g^{-1}). Moreover, the distribution of the binding sites in the imprinted polymer should indicate a higher heterogeneity than in nonimprinted. Thereby, MMC-MIP renders smaller m values. Thus, imprinted polymers synthesized according to this methodology showed a significant imprinting factor due to the differences observed between MIP vs NIP.

To evaluate the selectivity of the MIPs created by microwave induction, a cross-reactivity study was performed with three different fluorophores. The fluorescein has a similar structure to rhodamine 6G. In contrast, curcumin and methylene blue have a completely different structure to R6G.

https://doi.org/10.1021/acsapm.3c03068
ACS Appl. Polym. Mater. 2024, 6, 3243−3252

Table 4. Adsorption Constant (K_a) and Binding Capacity ($\bar{N}$) of the High and Low Energy Binding Sites for R6G of the MMC-MIP and MMC-NIP Nanoparticles

polymer	K_a (mM^{-1})	N_{K1-K2} (μmol g−1)	m	a (μmol g^{-1} $(mM^{-1})^m$)	r^2
MMC-MIP	22 ± 2	470 ± 20	0.78 ± 0.01	102 ± 15	0.97
MMC-NIP	10 ± 1	10 ± 3	0.43 ± 0.02	54 ± 7	0.95

As can be seen in Figure S10, the results obtained for fluorescein, curcumin, and methylene blue show that the retention of these analytes by MIPs is nonspecific since the retentions by NIPs and MIPs are similar. This fact can be observed easily in terms of the imprinting factor (IF) from the graph, where the IF for R6G is 2.3, meaning that the retention of MIP is much higher than that of NIP, but for the rest of the analytes, the imprinted factor is close to 1, meaning that the binding of the analyte by the polymer is totally unspecific. In terms of the reusability of the material, it was observed that after 10 (Figure S11) cycles with the same material, there was no loss in the recognition properties. A comparison table with the advantages of the presented method is included in the Supporting Information Table S2.[35−42]

Magnetic Characterization. Finally, we have measured the magnetic properties of the iron oxide core to check whether the magnetic properties were affected by the polymerization process. Figure 8 summarizes the magnetic

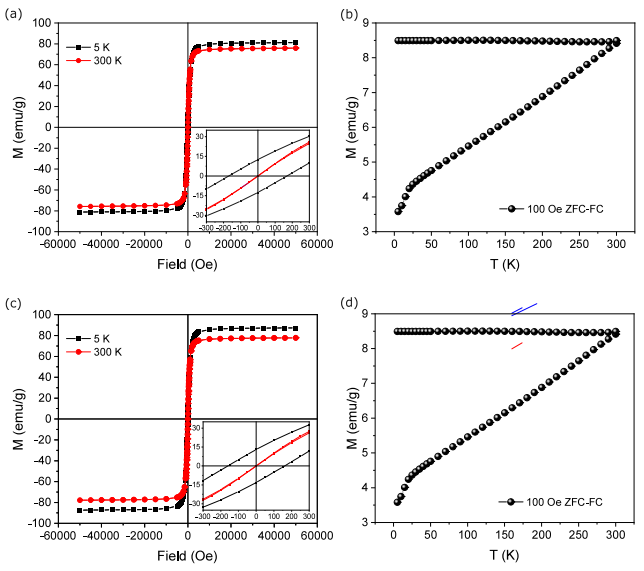

Figure 8. Hysteresis loop and thermal evolution of magnetization for magnetic nanoparticles before (a) and (b) and after (c) and (d) the polymerization procedure.

properties of the nanoparticles before and after polymerization. From the figure, it is clear that both, hysteresis loops and thermal evolution of the magnetization are identical before and after the process, within the experimental error.

The hysteresis loops are typical of superparamagnetic materials: no coercivity or remanence is observed at room temperature, but an increase of both parameters is observed when measuring at low temperature. The thermal evolution of magnetization before and after polymerization was also very similar. In both cases, field-cooled and zero-field curves converged immediately above room temperature, which confirms that the blocking temperature did also not change by the effect of polymerization.

CONCLUSIONS

Microwave radiation has been successfully applied for coating magnetic multicore (MMC) nanoparticles with a molecularly imprinted polymer (MIP). The proposed method uses microwave radiation for direct polymerization of the MIP on the surface of the MMC nanoparticles rather than in solution, making the process highly efficient by decreasing the nonspecific interactions of polymer material not bound to the nanoparticles. The method allows facile variation of polymerization parameters such as volume, stirring, reaction time, or temperature, making it highly versatile. Consequently, control of the resulting thickness of the MIP is achieved, while avoiding the formation of agglomerates that reduce the surface area of the molecular recognition. In-depth characterization of the atomic- and nanostructure of the MMC nanoparticles before and after polymerization shows that the reported molecular imprinting process does not induce structural changes in the MMC nanoparticles, making it highly relevant for the general scientific community since there is a high chance it could be effectively used for polymerizing other magnetic systems without inducing changes in their structure or properties. The produced MMC-MIP nanoparticles exhibit fast binding kinetics, high binding capacity, and selectivity toward the template molecule and can be easily recovered for reuse due to the magnetic nature of the core nanoparticles, showing no loss in the recognition properties after 10 cycles.

ASSOCIATED CONTENT

Supporting Information

The Supporting Information is available free of charge at https://pubs.acs.org/doi/10.1021/acsapm.3c03068.

Structure of the rhodamine 6G (R6G) molecule (Figure S1), face-centered central composite experimental runs in the experimental design (Table S1), normal probability plot of the studentized residuals (Figure S2), actual vs predicted thickness of the MIP layer plot (Figure S3), Rietveld refinement of PXRD data collected on MMC (Figure S4) and MMC-MIP nanoparticles (Figure S5) nanoparticles, modeled as (a) magnetite Fe_3O_4 (b) maghemite γ-Fe_2O_3 and (c) nonstoichiometric Fe_xO_4, Rietveld refinement of PXRD data collected on the MMC sample modeled using (a) the nonstoichiometric Fe_xO_4 and (b) a combination of Fe_xO_4 and vacancy ordered γ-Fe_2O_3 in space group $P4_32_12$ (Figure S6), FTIR spectra of the MMC nanoparticles before and after MIP coating (Figure S7), histograms of distribution size of the Fe_3O_4 nanoparticles (Figure S8), adsorption kinetics of R6G (Figure S9), cross-reactivity for the study of MIP selectivity toward rhodamine 6G against other fluorophores (Figure 10) and chormatograms and repeatability test (Figure S11) (PDF)

https://doi.org/10.1021/acsapm.3c03068
ACS Appl. Polym. Mater. 2024, 6, 3243−3252

AUTHOR INFORMATION

Corresponding Authors

Lucas Pérez − *Departamento de Física de Materiales, Universidad Complutense de Madrid, Madrid 28040, Spain; Instituto Madrileño de Estudios Avanzados, IMDEA Nanociencia,, Madrid 28049, Spain; Surface Science and Magnetism of Low Dimensional Systems, Universidad Complutense de Madrid, Madrid 28040, Spain;* orcid.org/0000-0001-9470-7987; Email: lucas.perez@ucm.es

Javier Lucas Urraca − *Chemical Optosensors and Applied Photochemistry Group (GSOLFA), Departmento de Química Analítica. Facultad de Ciencias Químicas, Universidad Complutense de Madrid, Madrid 28040, Spain;* orcid.org/0000-0003-2843-0865; Email: jurracar@ucm.es

Authors

Miriam Guadaño-Sánchez − *Chemical Optosensors and Applied Photochemistry Group (GSOLFA), Departmento de Química Analítica. Facultad de Ciencias Químicas, Universidad Complutense de Madrid, Madrid 28040, Spain;* orcid.org/0000-0002-0895-9502

Fernando Navarro-Villoslada − *Chemical Optosensors and Applied Photochemistry Group (GSOLFA), Departmento de Química Analítica. Facultad de Ciencias Químicas, Universidad Complutense de Madrid, Madrid 28040, Spain;* orcid.org/0000-0002-6149-7511

Guiomar Delgado-Soria − *Instituto de Química Física "Blas Cabrera", Madrid 28006, Spain;* Present Address: Laboratorio Nacional de Fusión, CIEMAT, 28 040, Madrid, Spain

José. F. Marco − *Instituto de Química Física "Blas Cabrera", Madrid 28006, Spain*

Matilde Saura-Muzquiz − *Departamento de Física de Materiales, Universidad Complutense de Madrid, Madrid 28040, Spain*

Laura Álvaro-Gómez − *Departamento de Física de Materiales, Universidad Complutense de Madrid, Madrid 28040, Spain*

Patricia de la Presa − *Departamento de Física de Materiales, Universidad Complutense de Madrid, Madrid 28040, Spain; Instituto de Magnetismo Aplicado UCM-ADIF-CSIC, Universidad Complutense de Madrid, Las Rozas 28230, Spain;* orcid.org/0000-0002-9456-8320

Complete contact information is available at: https://pubs.acs.org/10.1021/acsapm.3c03068

Author Contributions

L.P., F.N.-V, and J.L.U. conceived and planned the experiments. F.N.-V. performed the formal analysis to optimize the experimental parameters for the synthesis of the nanomaterial. M.G.-S. and J.L.U. synthesized the nanomaterials and carried out chromatography and equilibrium binding experiments. J.L.U. carried out the TEM experiments. J.F.M. and G.D.-S. performed the Mossbauer spectroscopy and P.P. and L.A.-G. the magnetic characterization. M.S.-M. analyzed the PXRD data. F.N.-V., L.P., and J.L.U. wrote the paper with input from all authors. All authors have approved the final version of the manuscript.

Notes

The authors declare no competing financial interest.

ACKNOWLEDGMENTS

This work has been partially funded by MCIN/AEI/10.13039/501100011033 through projects PID2021-127457OB-C21/C22 and TED2021-130957B-C52. We thank the Spanish National Center of Electron Microscopy for Scanning Electron Microscopy measurements and the CAI de difracción de rayos X of Universidad Complutense de Madrid for X-ray diffraction measurements. M.S.-M. acknowledges the financial support from the Comunidad de Madrid, Spain, through an "Atracción de Talento Investigador" fellowship (2020-T2/IND-20581).

REFERENCES

(1) Haupt, K.; Mosbach, K. Molecularly imprinted polymers and their use in biomimetic sensors. *Chem. Rev.* **2000**, *100*, 2495−2504.

(2) Remcho, V. T.; Tan, Z. J. MIPs as chromatographic stationary phases for molecular recognition. *Anal. Chem.* **1999**, *71*, 248A−255A.

(3) He, S.; Zhang, L.; Bai, S.; Yang, H.; Cui, Z.; Zhang, X.; Li, Y. Advances of molecularly imprinted polymers (MIP) and the application in drug delivery. *Eur. Polym. J.* **2021**, *143*, 110179.

(4) Alexander, C.; Davidson, L.; Hayes, W. Imprinted polymers: Artificial molecular recognition materials with applications in synthesis and catalysis. *Tetrahedron* **2003**, *59*, 2025−2057.

(5) Haupt, K. *Molecular imprinting*; Springer: Berlin, Heidelberg, 2012.

(6) Hajne, J.; Hanson, K. L.; van Zalinge, H.; Nicolau, D. V. Motility of actin filaments on micro-contact printedmyosin patterns. *IEEE Trans. NanoBiosci.* **2015**, *14*, 313−322.

(7) Paul, K. E.; Zhu, C.; Love, J. C.; Whitesides, G. M. Fabrication of mid-infrared frequency-selective surfaces by soft lithography. *Appl. Opt.* **2001**, *40*, 4557−4561.

(8) Fuchs, Y.; Soppera, O.; Haupt, K. Photopolymerization and photostructuring of molecularly imprinted polymers for sensor applications−A review. *Anal. Chim. Acta* **2012**, *717*, 7−20.

(9) Boysen, R. I.; Schwarz, L. J.; Nicolau, D. V.; Hearn, M. T. Molecularly imprinted polymer membranes and thin films for the separation and sensing of biomacromolecules. *J. Sep. Sci.* **2017**, *40*, 314−335.

(10) Mayes, A. G.; Mosbach, K. Molecularly Imprinted Polymer Beads: Suspension Polymerization Using a Liquid Perfluorocarbon as the Dispersing Phase. *Anal. Chem.* **1996**, *68*, 3769−3774.

(11) Schmidt, R. H.; Mosbach, K.; Haupt, K. A simple method for spin-coating molecularly imprinted polymer films of controlled thickness and porosity. *Adv. Mater.* **2004**, *16*, 719−722.

(12) Greiner, A.; Wendorff, J. H. Electrospinning: a Fascinating Method for the Preparation of Ultrathin Fibers, Angew. *Chem. Int. Ed.* **2007**, *46*, 5670−5703.

(13) Matyjaszewski, K.; Davis, T. P. *Handbook of Radical Polymerization*; John Wiley & Sons, 2000; **pp.** 117187.

(14) Braunecker, W. A.; Matyjaszewski, K. Controlled/living radical polymerization: Features, developments, and perspectives, Prog. *Polym. Sci.* **2007**, *32*, 93−146.

(15) Londoño-Navarro, J.; Riaño-Rojas, J. C.; Restrepo-Parra, E. Competition between anisotropy and dipolar interaction in multicore nanoparticles: Monte Carlo simulation. *DYNA.* **2015**, *82*, 66.

(16) Dutz, S.; Kettering, M.; Hilger, I.; Müller, R.; Zeisberger, M. Magnetic Multicore Nanoparticles for Hyperthermia - Influence of Particle Immobilization in Tumour Tissue on Magnetic Properties. *Nanotechnology* **2011**, *22*, 265102.

(17) Schaller, V.; Wahnström, G.; Sanz-Velasco, A.; Enoksson, P.; Johansson, C. Monte Carlo simulation of magnetic multi-core nanoparticles. *J. Mag. Mag. Mater.* **2019**, *321*, 1400−1403.

(18) Niu, M.; Pham-Huy, C.; He, H. Core-shell nanoparticles coated with molecularly imprinted polymers: A review. *Microchim. Acta* **2016**, *183*, 2677−2695.

(19) Tan, C. J.; Chua, H. G.; Ker, K. H.; Tong, Y. W. Preparation of bovine serum albumin surface-imprinted submicrometer particles with

magnetic susceptibility through core-shell miniemulsion polymerization. *Anal. Chem.* **2008**, *80*, 683−692.
(20) Kong, X.; Gao, R.; He, X.; Chen, L.; Zhang, Y. Synthesis and characterization of the core−shell magnetic molecularly imprinted polymers (Fe3O4@MIPs) adsorbents for effective extraction and determination of sulfonamides in the poultry feed. *J. Chromatogr. A* **2012**, *1245*, 8−16.
(21) Fan, J. P.; Xu, X. K.; Xu, R.; Zhang, X. H.; Zhu, J. H. Preparation and characterization of molecular imprinted polymer functionalized with core/shell magnetic particles (Fe3O4@SiO2@MIP) for the simultaneous recognition and enrichment of four taxoids in Taxus × media. *Chem. Engin. J.* **2015**, *279*, 567−577.
(22) Mehmet, D.; Cem, E.; Boris, M. Recent advances on core−shell magnetic molecularly imprinted polymers for biomacromolecules. *TrAC Trends Anal. Chem.* **2019**, *114*, 202−217.
(23) Urraca, J. L.; Barrios, C. A.; Canalejas-Tejero, V.; Orellana, G.; Moreno-Bondi, M. C. Molecular Recognition with Nanostructures Fabricated by Photopolymerization within Metallic Subwavelength Apertures. *Nanoscale* **2014**, *6*, 8656−8663.
(24) Rodríguez-Carvajal, J. An Introduction to the Program FullProf 2000. In *Laboratoire Léon Brillouin (CEA-CNRS)*; CEA/Saclay, 91191 Gif sur Yvette Cedex: France, 2001.
(25) Thompson, P.; Cox, D. E.; Hastings, J. B. Rietveld refinement of Debye−Scherrer synchrotron X-ray data from Al_2O_3. *J. Appl. Crystallogr.* **1987**, *20*, 79−83.
(26) ISO 5725−5:1998(E). *Accuracy (trueness and precision) of measurement methods and results. Part 5: alternative methods for the determination of the precision of a standard measurement method*; International Organization for Standardization: Geneva, Switzerland, 1998.
(27) Braun, P. B. A Superstructure in Spinels. *Nature* **1952**, *170* (4339), 1123−1123.
(28) Greaves, C. A powder neutron diffraction investigation of vacancy ordering and covalence in γ-Fe_2O_3. *J. Solid State Chem.* **1983**, *49* (3), 325−333.
(29) Shmakov, A. N.; Kryukova, G. N.; Tsybulya, S. V.; Chuvilin, A. L.; Solovyeva, L. P. Vacancy Ordering in [gamma]-Fe_2O_3: Synchrotron X-ray Powder Diffraction and High-Resolution Electron Microscopy Studies. *J. Appl. Crystallogr.* **1995**, *28* (2), 141−145.
(30) Andersen, H. L.; Frandsen, B. A.; Gunnlaugsson, H. P.; Jorgensen, M. R. V.; Billinge, S. J. L.; Jensen, K. M. O.; Christensen, M. Local and long-range atomic/magnetic structure of non-stoichiometric spinel iron oxide nanocrystallites. *IucrJ* **2021**, *8* (1), 33−45.
(31) Goya, G. F.; Berquo, T. S.; Fonseca, F. C.; Morales, M. P. Static and dynamic magnetic properties of spherical magnetite nanoparticles. *J. Appl. Phys.* **2003**, *94*, 3520.
(32) Roca, A. G.; Marco, J. F.; Morales, M. P.; Serna, C. J. Effect of Nature and Particle Size on Properties of Uniform Magnetite and Maghemite Nanoparticles. *J. Phys. Chem. C* **2007**, *111*, 18577−18584.
(33) Vandenberghe, E.; Barrero, C. A.; da Costa, G. M.; Van San, E.; De Grave, E. Mössbauer characterization of iron oxides and (oxy)hydroxides: the present state of the art. *Hyperfine Interact.* **2000**, *126*, 247−259.
(34) García-Calzón, J. A.; Díaz-García, M. E. Characterization of binding sites in molecularly imprinted polymers, Sens. *Actuators B* **2007**, *123*, 1180−1194.
(35) Kuhn, J.; Aylaz, G.; Sari, E.; Marco, M.; Yiu, H. H. P.; Duman, M. Selective binding of antibiotics using magnetic molecular imprint polymer (MMIP) networks prepared from vinyl-functionalized magnetic nanoparticles. *J. Hazard. Mater.* **2020**, *387*, 121709.
(36) Turan, E.; Şahin, F. Molecularly imprinted biocompatible magnetic nanoparticles for specific recognition of Ochratoxin A. *Sens. Actuators B: Chem.* **2016**, *227*, 668−676.
(37) Santos, A. C. F.; de Araújo, O. R. P.; Moura, F. A.; Khan, S.; Tanaka, A. A.; Santana, A. E. G.; Pividori, M. I.; Taboada-Sotomayor, M. D. P.; Goulart, M. O. F. Development of magnetic nanoparticles modified with new molecularly imprinted polymer (MIPs) for selective analysis of glutathione. *Sens. Actuators B: Chem.* **2021**, *344*, 130171.
(38) Fan, J.-P.; Xu, X.-K.; Xu, R.; Zhang, X.-H.; Zhu, J.-H. Preparation and characterization of molecular imprinted polymer functionalized with core/shell magnetic particles (Fe_3O_4 @SiO_2 @MIP) for the simultaneous recognition and enrichment of four taxoids in Taxus × media. *J. Chem. Eng.* **2015**, *279*, 567−577.
(39) Zeb, S.; Wong, A.; Khan, S.; Hussain, S.; Sotomayor, M. D. P. T. Using magnetic nanoparticles/MIP-based electrochemical sensor for quantification of tetracycline in milk samples. *J. Electroanal. Chem.* **2021**, *900*, 115713.
(40) Calahorra-Rio, L.; Guadaño-Sánchez, M.; Moya-Cavas, T.; Urraca, J. L. Magnetic Core-Shell Nanoparticles Using Molecularly Imprinted Polymers for Zearalenone Determination. *Molecules* **2022**, *27*, 8166.
(41) Lafuente-González, E.; Guadaño-Sánchez, M.; Urriza-Arsuaga, I.; Urraca, J. L. Core-Shell Magnetic Imprinted Polymers for the Recognition of FLAG-Tagpeptide. *Int. J. Mol. Sci.* **2023**, *24*, 3453.
(42) Li, Y.; Ding, M. J.; Wang, S.; Wang, R. Y.; Wu, X. L.; Wen, T. T.; Yuan, L. H.; Dai, P.; Lin, Y. H.; Zhou, X. M. Preparation of imprinted polymers at surface of magnetic nanoparticles for the selective extraction of tadalafil from medicines. *ACS Appl. Mater. Interfaces* **2011**, *3*, 3308−3315.

https://doi.org/10.1021/acsapm.3c03068
ACS Appl. Polym. Mater. 2024, 6, 3243−3252